Fault diagnostics of realistic arrays from a reduced number of phaseless near field measurements

Fault Diagnosis of Realistic Arrays from a Reduced Number of Phaseless Near-Field Measurements

Roberta Palmeri, *Member IEEE*, Giada Maria Battaglia, *Member IEEE*, Andrea Francesco Morabito, Sandra Costanzo, *Senior Member, IEEE*, Francesca Venneri, and Tommaso Isernia, *Fellow, IEEE*

***Abstract*—We present a new approach to the problem of detecting element failures in any kind of array antenna. The proposed method requires only phaseless information on the generated field and reduces as much as possible the number of needed measurements by exploiting the Compressed Sensing (CS) theory. The solution procedure works regardless of whether the probes are located in the near-field or far-field region of the antenna under test, and it is the first and only CS-based technique able to perform the diagnostics by exploiting only phaseless measurements taken exclusively in the near-field zone. It also results simple and fast as it requires a single measurement surface and reduces, in most practical instances, to the solution of a convex programming problem. The given theory is supported by very many numerical experiments involving full-wave electromagnetic simulations of realistic arrays and considering both scalar and vector fields with different types of scanning surfaces and different noise levels. Both ON-OFF and phase faults are dealt with. An experimental validation on a fabricated array is also presented.**

***Index Terms*—Array antennas, compressed sensing, fault diagnosis.**

I. Introduction

The increasingly high performance requirements for array antennas in current applications makes it necessary to monitor their radiating elements in a fast and effective fashion. For this reason, several methods have been devised to identify faulty elements by resorting to far-field (e.g., [1]–[11]) and near-field (e.g., [12]–[18]) measurements.

Most of these techniques require the acquisition of both the amplitude and phase of the generated field (see, for instance, [1]–[6],[12]–[17]). This enables casting the diagnostics problem as a *linear* one, improving the accuracy and efficiency of the solution while also avoiding the adoption of two or more measurement surfaces.

On the other hand, phase measurements can be inconvenient (or even unfeasible) in many cases, including environments with poor thermal stability [19] or applications where measurements must be taken by unmanned aerial vehicles [20]. Moreover, while measuring the field amplitude is relatively simple at all frequencies, phase acquisition can be difficult in high-frequency scenarios, e.g., applications involving millimeter and submillimeter waves [19]–[22].

Difficulties inherent to phase measurements led the authors in [10] and [11] to introduce two new approaches to detect ON-OFF element failures of array antennas from *amplitude-only* far-field data. Notably, despite the nonlinearity of the underlying optimization problem induced by the adoption of phaseless measurements, these two techniques allowed for the exploitation of the compressive sensing theory developed in [23], considerably reducing the number of needed measurements with respect to usual approaches. In particular, the methods in [10] and [11] overcame, for the first time in the array fault diagnosis literature, the usual limitation of applying CS theory only if both amplitude and phase measurements of the radiated field are available. Furthermore, provided that the percentage of faulty elements is not so high, the two techniques cast the diagnostics as a convex programming (CP) problem guaranteeing the fast achievement of the optimal solution without relying to computationally expensive global optimization algorithms.

Unfortunately, the approaches in [10] and [11] can only be applied when far-field measurements are available, and hence the near-field case is systematically addressed by exploiting *amplitude* and *phase* measurements (see, for instance, [12]–[17]). This means that techniques allowing array diagnostics by exploiting only phaseless measurements taken exclusively in the near-field zone are still lacking[1], the sole exceptions being the two methods presented in [8] and [18]. However, these two techniques have a computational burden much larger than that of the procedures developed in [10] and [11]. In fact, [8] and [18] relied on hybrid evolutionary algorithms and artificial neural networks (ANNs), respectively, which introduce the intrinsic computational complexity of global-optimization algorithms and the extra computational cost required for training ANNs. Moreover, [8] and [18] required a significantly larger number of measurements than those used in [10] and [11]

R. Palmeri is with the Institute for the Electromagnetic Sensing of the Environment of the CNR, Napoli, Italy. G. M. Battaglia, A. F. Morabito, and T. Isernia are with Università di Reggio Calabria, Italy. S. Costanzo and F. Venneri are with Università della Calabria, Rende, Italy. All authors are also with Consorzio Nazionale Interuniversitario per le Telecomunicazioni, Parma, Italy. *Corresponding author*: A. F. Morabito (andrea.morabito@unirc.it).

[1] Few contributions associated with phase retrieval (e.g., [24],[25]) can also be found but, unlike the method presented here, they exploit multiple measurement surfaces.

for data acquisition, with an inherent negative impact on the overall diagnostics time.

To address this gap, in the following, we present an approach to the fault diagnosis of array antennas that exploits only (a reduced number of) phaseless measurements taken entirely in the near-field region.

The proposed method represents the final generalization of the techniques developed in [10] and [11] for failure diagnosis using amplitude-only field measurements. In fact, while [11] extended the theory developed in [10] from 1-D 'ideal' arrays whose radiated field is given by the array factor to 'realistic' planar and conformal arrays, the present work extends the one in [11] by removing the limitation of needing measurements taken in the far-field zone.

As a further innovation with respect to the technique in [11], the present approach is developed not only by exploiting the active element patterns (AEPs), but also by introducing a new fruitful formulation of the problem for the case where AEPs are not available. This is achieved by utilizing a matrix relationship between data and unknowns, which simplifies the process of diagnosing realistic arrays.

Finally, while the technique in [11] works just on scalar fields and can only detect ON-OFF faults, the proposed approach can also be applied to vector fields (thus enabling the diagnostics of more complex arrays with nondominant field components) and can detect both ON-OFF and phase faults.

Like its two predecessors proposed in [10] and [11], the new method is able to alleviate the ill-posedness of the problem by exploiting the CS theory and optimally solving it as a CP problem in most practical instances. Consequently, its computational burden is significantly lower than the one of the (only two) other available approaches able to solve the specific problem at hand (i.e., the techniques in [8] and [18] recalled above). Additionally, opposite to essentially all the approaches based on phaseless data (which need two different sets of measurements – see [26] for more details), the proposed method just requires a single measurement surface.

In the following, the diagnostics approach is presented in Section II. Then, it is assessed both numerically (in Section III) and experimentally (in Section IV). Conclusions follow.

II. The Diagnostic Procedure

To present the new diagnostics technique, let us consider a completely arbitrary array under test (AUT) composed of N (possibly different) radiating elements spatially arranged into a layout having any shape and interelement distance. As long as all radiating elements are correctly working, the AUT will be denoted as "gold" AUT, while if S of its elements are not correctly working, it will be denoted as "faulty" AUT.

Moreover, let us consider a virtual array, denoted as the "differential" AUT, which is identical to the "gold" AUT but for the fact that its element excitations are equal to the difference between the "gold" and "faulty" AUT element excitations.

Starting from the knowledge of the "gold" AUT, the approach is aimed at identifying the nonworking elements by exploiting only phaseless measurements of the "faulty" AUT's field and at reducing the number of required measurements as much as possible by using CS theory.

While the adopted solution procedure is applicable to the cases of both near-field and far-field measurements, in the following its presentation and assessment will be made by exclusively considering near-field measurements. In fact, this scenario is much more challenging than the one with far-field measurements, as the latter may lead to a Fourier representation of the field which allows the exploitation of CS theoretical results guaranteeing effectiveness [10].

The solution procedure works regardless of whether the AEPs of the "gold" AUT are known, and can be used to detect both ON-OFF and phase faults. To show these additional qualities, in the following, the approach will be first presented by relying on the AEPs' knowledge and respectively addressing, in subsections II.A and II.B, the detection of ON-OFF faults and phase faults. Then, in subsection II. C, the case where the diagnostics cannot rely on the AEPs will be addressed.

II.A. Detection of ON-OFF faults (by exploiting AEPs)

A common issue occurring in large arrays is the complete break of one or more radiating elements. This is the case for "ON-OFF" faults, corresponding to a "faulty" AUT having a null excitation on S of its elements.

To solve the diagnostics problem in this scenario, let us denote with $\boldsymbol{E}^G(\boldsymbol{r})$ and $\boldsymbol{E}^F(\boldsymbol{r})$ the vector fields generated by the "gold" and "faulty" AUTs, respectively, $\boldsymbol{r} = [x, y, z]$ being the vector spanning the observation space, i.e.,

$$\boldsymbol{E}^G(\boldsymbol{r}) = \sum_{n=1}^{N} I_n^G \boldsymbol{\psi}_n(\boldsymbol{r}) \tag{1.a}$$

$$\boldsymbol{E}^F(\boldsymbol{r}) = \sum_{n=1}^{N} I_n^F \boldsymbol{\psi}_n(\boldsymbol{r}) \tag{1.b}$$

I_n^G and I_n^F are the excitation of the n-th element of the "gold" and "faulty" AUTs, respectively, while $\boldsymbol{\psi}_n$ denotes the vector AEP of the n-th element, i.e., the field generated by the "gold" array when only the n-th element is excited (with I_n^G=1) and all the others are connected to matching loads [27].

Then, at any generic measurement point $\boldsymbol{r}_m$, the following relationship will hold true:

$$|\boldsymbol{E}^F(\boldsymbol{r}_m)|^2 - |\boldsymbol{E}^G(\boldsymbol{r}_m)|^2 = |\Delta\boldsymbol{E}(\boldsymbol{r}_m)|^2 + \boldsymbol{\alpha}_m \tag{2.a}$$

with:

$$\boldsymbol{\alpha}_m = -2Re\langle \boldsymbol{E}^G(\boldsymbol{r}_m), \Delta\boldsymbol{E}(\boldsymbol{r}_m)\rangle \tag{2.b}$$

$$\Delta\boldsymbol{E}(\boldsymbol{r_m}) = \boldsymbol{E^G}(\boldsymbol{r_m}) - \boldsymbol{E^F}(\boldsymbol{r_m}) \tag{2.c}$$

$$\Delta\boldsymbol{E}(\boldsymbol{r}_m) = \sum_{n=1}^{N} \Delta I_n \boldsymbol{\psi}_n(\boldsymbol{r}_m) \tag{2.d}$$

$$\Delta I_n = I_n^G - I_n^F \quad n = 1, \dots, N \tag{2.e}$$

(2.d) and (2.e) denoting the field and excitations of the "differential" AUT, respectively.

The goal of the diagnostics procedure is to retrieve $\underline{\Delta I} =$

$[\Delta I_1,\ldots,\Delta I_N]$ from the knowledge of the "gold" AUT and of $|\boldsymbol{E}^F|^2$ in a measurement set composed of M points $\boldsymbol{r_1},\ldots,\boldsymbol{r_M}$ located in the near-field zone and chosen, by recurring to only one surface, according to some convenient rule (see for instance in [28]-[31]). In fact, since the "gold" AUT is assumed to be known, determining $\underline{\Delta I}$ is equivalent to identify $I_1^F,\ldots, I_N^F$ and hence to detect the faulty elements.

The case of ON-OFF faults corresponds to $I_n^F = 0$ for all the n values identifying the S malfunctioning elements. Therefore, only S elements of $\underline{\Delta I}$ are different from zero and hence, provided that S is much lower than N (which is usually the case), the vector $\underline{\Delta I}$ is *sparse*. This property suggests the adoption of CS as a powerful tool for the diagnosis. In particular, by using the subscripts μ and ν to distinguish the two components[2] of the vector fields tangential to the measurement surface, the diagnostics can be performed by identifying $\underline{\Delta I}$ as the solution of the following optimization problem:

$$\min_{\Delta I_1,\ldots,\Delta I_N} \left\|\underline{\Delta I}\right\|_1 \tag{3.a}$$

subject to:

$$\left\| \frac{\left|E_\mu^F(\boldsymbol{r_m})\right|^2 - \left|E_\mu^G(\boldsymbol{r_m})\right|^2 - \alpha_{\mu m} - \left|\Delta E_\mu(\boldsymbol{r_m})\right|^2}{\left|E_\mu^G(\boldsymbol{r_m})\right|^2} \right\|_2 < \varepsilon \tag{3.b}$$

$$\left\| \frac{|E_\nu^F(\boldsymbol{r_m})|^2 - |E_\nu^G(\boldsymbol{r_m})|^2 - \alpha_{\nu m} - |\Delta E_\nu(\boldsymbol{r_m})|^2}{|E_\nu^G(\boldsymbol{r_m})|^2} \right\|_2 < \varepsilon \tag{3.c}$$

with:

$$\alpha_{\mu m} = -2Re\langle E_\mu^G(\boldsymbol{r_m}), \Delta E_\mu(\boldsymbol{r_m})\rangle \tag{3.d}$$

$$\alpha_{\nu m} = -2Re\langle E_\nu^G(\boldsymbol{r_m}), \Delta E_\nu(\boldsymbol{r_m})\rangle \tag{3.e}$$

The effectiveness of the formulation (3.a)–(3.e) is boosted by the condition $S \ll N$, which is the case in most actual applications (see, for instance, [10] and the references cited therein). In fact, this condition ensures that two crucial circumstances come into play, as detailed in the following.

First, since the unknown is sparse, the CS framework can be profitably applied[3]. In fact, minimization (3.a) is aimed at enforcing the sparsity of the solution, while constraints (3.b) and (3.c) ensure the fulfillment of equation (2.a) with a tolerance equal to ε (which is a small, real and positive constant chosen by the user).

Second, $|\Delta\boldsymbol{E}(\boldsymbol{r_m})|^2$ is small with respect to $\boldsymbol{\alpha_m}$ for $m = 1,\ldots,M$. This circumstance, which can be further consolidated by performing the measurements at those points where $\boldsymbol{E}^G$ has a larger intensity, entails that (3.b) and (3.c) basically act as 'quadratic' constraints, and hence optimization (3) can be considered a CP problem. This brings decisive advantages in terms of both computational burden and optimality (unicity) of the solution, whose identification will be guaranteed even by using fast local-optimization procedures.

By virtue of all the above, the approach keeps all the advantages of its predecessors [10] and [11] (i.e., the smart adoption of the 'sparsity' concept, the reduced computational burden supplied by the CP formulation, the requirement of only one measurement surface and of only phaseless field data) while simultaneously extending them to the important scenario where the measurements can be taken only in the near-field zone.

II.B. Detection of phase faults (by exploiting AEPs)

In addition to ON-OFF faults, it is not unlikely that an incorrect value of the phase of the excitation coefficients is also produced. This kind of failure, which will henceforth be referred to as a "phase" fault, can be caused by many factors, such as faults in the beam-forming network and the adoption of digital phase shifters [8].

Interestingly, to detect possible phase faults, one just needs to adapt the diagnostics procedure presented in subsection II. A by modifying (3.a) as:

$$\min_{\Delta I_1,\ldots,\Delta I_N} \left\{ \left\|Real\left(\underline{\Delta I}\right)\right\|_1 + \left\|Imag\left(\underline{\Delta I}\right)\right\|_1 \right\} \tag{4}$$

and adding to (3.b) and (3.c) the following constraint:

$$|\Delta I_n|^2 - 2Real\{I_n^G \Delta I_n^*\} \le 0, \quad n = 1,\ldots,N \tag{5}$$

In fact, all the properties and capabilities of problem formulation (3) still hold true, but the new objective function enforces the sparsity of both the real and imaginary parts of the "differential" AUT excitations.

As far as the additional constraint (5) is concerned, it is worth noting that it corresponds to enforce $|I_n^F|^2 \le |I_n^G|^2$ for $n = 1,\ldots,N$. This inequality, which represents a convex set in terms of the unknowns, further improves the algorithm convergence by effectively reducing the research space.

As will be shown in Section III, the adoption of (4) and (5) allows for accurately detecting even low phase errors and retrieving the exact complex value of the AUT's excitations.

II.C. Experimentally-oriented procedure not recurring to AEPs

If AEPs are not available or cannot be evaluated due to a simultaneous excitation of all the array elements (as occurs, for instance, in slotted waveguide arrays and reflectarrays), the two formulations presented in subsections II.A and II.B cannot be used in a straightforward fashion. To overcome this issue, a third formulation of the proposed approach is introduced in the following.

To this end, let us first consider the general linear equation adopted in [14] to express the relationship among the AUT elements' excitations (say $\underline{x} \in C^N$) and the voltage measured on the observation domain (say $\underline{y} \in C^M$):

$$\underline{\underline{A}}\,\underline{x} = \underline{y} \tag{6}$$

where the matrix $\underline{\underline{A}}$ takes into account both the electric-field

[2] Depending on the chosen measurement set-up, μ and ν can be x and y (for planar scanning), z and φ (for cylindrical scanning), or θ and φ (for spherical scanning).

[3] It can reasonably be expected that the incoherence property demonstrated in [10] keeps verified as long as the measurements placement assures a low spatial correlation among data [13].

radiation pattern of the n-th radiating element of the AUT, say $\boldsymbol{f}_n(\theta,\varphi)$, as well as the effective height of the measuring probe, say $\boldsymbol{h}_n(\theta,\varphi)$[4]. In particular, $\underline{\underline{A}} \in C^{M\times N}$ is a matrix whose (m,n)-th element is equal to $exp(-j\beta r_{m,n})/(4\pi r_{m,n})\boldsymbol{f}_n(\theta_{m,n},\varphi_{m,n})\cdot\boldsymbol{h}_n(\theta'_{m,n},\varphi'_{m,n})$, where $r_{m,n}$ denotes the distance between the m-th measurement point and the n-th element of the AUT, while $\theta_{m,n}$ and $\varphi_{m,n}$ are the elevation and azimuth angles between the m-th measurement point and the n-th element position in a reference system centered on the n-th array radiating element[5]. For the sake of clarity, the defined variables as well as $\theta'_{m,n}$ and $\varphi'_{m,n}$ are depicted in Fig. 1.

Then, to extend the method presented in subsection II.A to the case where the AEPs are not available, one just needs to reconsider (2) by expressing the fields generated by the "gold" and "faulty" AUTs as dictated by (6). Therefore, by using the superscripts *G* and *F* to distinguish the excitations and fields relative to the "gold" and the "faulty" AUTs, respectively, and performing the square amplitude of the following relation,

$$\underline{\mathrm{y}}^{\mathrm{F}} = \underline{\mathrm{y}}^{\mathrm{G}} - \underline{\Delta\mathrm{y}} \tag{7}$$

where $\underline{\mathrm{y}}^{\mathrm{G}}$ and $\underline{\Delta\mathrm{y}}$ are derived from (6), one obtains:

$$\underline{\mathrm{z}}^{\mathrm{F}} = \underline{\mathrm{z}}^{\mathrm{G}} + \underline{\Delta\mathrm{z}} - \left[\underline{\underline{\mathrm{A}}}\,\underline{\mathrm{x}}^{\mathrm{G}}\right]\circ\left[\underline{\underline{\mathrm{A}}}\,\underline{\Delta\mathrm{x}}\right]^{*} - \left[\underline{\underline{\mathrm{A}}}\,\underline{\Delta\mathrm{x}}\right]\circ\left[\underline{\underline{\mathrm{A}}}\,\underline{\mathrm{x}}^{\mathrm{G}}\right]^{*} \tag{8.a}$$

where $*$ denotes the complex conjugate, $\circ$ denotes the Hadamard product between vectors, and

$$\underline{z}^{\mathrm{F}} = \underline{\mathrm{y}}^{\mathrm{F}}\circ\underline{\mathrm{y}}^{\mathrm{F}^{*}} \tag{8.b}$$

$$\underline{\mathrm{z}}^{\mathrm{G}} = \underline{\mathrm{y}}^{\mathrm{G}}\circ\underline{\mathrm{y}}^{\mathrm{G}^{*}} \tag{8.c}$$

$$\underline{\Delta\mathrm{z}} = \left[\underline{\underline{\mathrm{A}}}\,\underline{\Delta\mathrm{x}}\right]\circ\left[\underline{\underline{\mathrm{A}}}\,\underline{\Delta\mathrm{x}}\right]^{*} = \underline{\Delta\mathrm{y}}\circ\underline{\Delta\mathrm{y}}^{*} \tag{8.d}$$

$$\underline{\Delta\mathrm{x}} = \underline{\mathrm{x}}^{\mathrm{G}} - \underline{\mathrm{x}}^{\mathrm{F}} \tag{8.e}$$

Finally, the optimization problem is recast as follows:

$$\min_{\Delta x_1,\ldots,\Delta x_N} \left\|\underline{\Delta\mathrm{x}}\right\|_1 \tag{9.a}$$

subject to:

$$\left\|\underline{\mathrm{z}}^{\mathrm{G}} + \underline{\Delta\mathrm{z}} - \left[\underline{\underline{\mathrm{A}}}\,\underline{\mathrm{x}}^{\mathrm{G}}\right]\circ\left[\underline{\underline{\mathrm{A}}}\,\underline{\Delta\mathrm{x}}\right]^{*} - \left[\underline{\underline{\mathrm{A}}}\,\underline{\Delta\mathrm{x}}\right]\circ\left[\underline{\underline{\mathrm{A}}}\,\underline{\mathrm{x}}^{\mathrm{G}}\right]^{*} - \underline{\mathrm{z}}^{\mathrm{F}}\right\|_2 < \varepsilon \tag{9.b}$$

Notably, formula (9) retains the advantages of optimization problem (3), including the possible reduction to a CP problem as well as its applicability to vector fields. Furthermore, similarly to (3), it can be easily extended to the case of phase faults by applying the rules reported in subsection II.B.

The actual performance of this solution procedure will be analyzed in Section IV through an experimental validation performed on a fabricated AUT by measuring $\underline{\mathrm{y}}^{\mathrm{F}}$ and $\underline{\mathrm{y}}^{\mathrm{G}}$ inside an anechoic chamber.

[4] The measurement surface is in the near-field region of the overall array and, at the same time, in the far-field region of the single array elements.

III. Numerical Assessment

In this Section, we present the outcomes of an extensive set of numerical experiments devoted to assessing the proposed diagnostic procedure. All test cases deal with realistic arrays whose generated field and AEPs have been computed exclusively by using full-wave electromagnetic simulations made through the CST Studio Suite software [32], and resort to *M* values much lower than the Nyquist one.

The excitation coefficients of the "gold" AUT has been set equal to 1 and, by virtue of the reasoning reported in Section II, only the field samples whose normalized square amplitude was larger than -25 dB have been taken into account as possible measurement points.

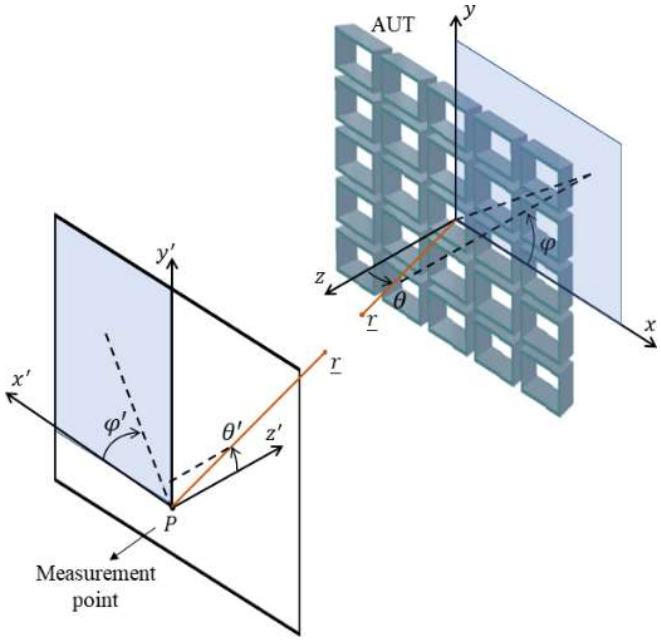

Fig. 1. Reference systems and variables involved in the diagnostics procedure of Sect. II.C.

All experiments have been performed by using only phaseless near-field measurements in cases of both noiseless and noisy data, and different types of measurement surfaces have been considered. The outcomes have been quantitatively evaluated by using the normalized mean square error (NMSE) definition in [11], i.e.,

$$NMSE = \frac{\left\|\underline{\Delta I} - \underline{\widehat{\Delta I}}\right\|_2^2}{\left\|\underline{\Delta I}\right\|_2^2} \tag{8}$$

$\underline{\Delta I}$ and $\underline{\widehat{\Delta I}}$ denote the vectors of the actual and retrieved "differential" AUT excitations, respectively.

The section is organized as follows.

First, in subsection III.A, ON-OFF faults are dealt with on both 1-D and 2-D AUTs by studying the Rate of Success of Excitations Recovery (RSER) and considering both cases of scalar and vector fields. The measurement surface was set as a

[5] $\boldsymbol{f}_n(\theta,\varphi)$ can be directly measured during the experiments, and $\boldsymbol{h}_n(\theta,\varphi)$ can also be simulated or analytically defined.

hemisphere in order to avoid losses of information due to its truncation.

Then, in subsection III.B, ON-OFF faults are again considered for 2-D AUTs and vector fields but, this time, using a planar measurement surface.

Finally, in subsection III.C, phase faults are dealt with by considering both cases of constant and random phase perturbations. A comparison with the method in [18] (which is the only recent technique able to address the diagnostics by using, as the present approach, only phaseless near-field measurements) is also included.

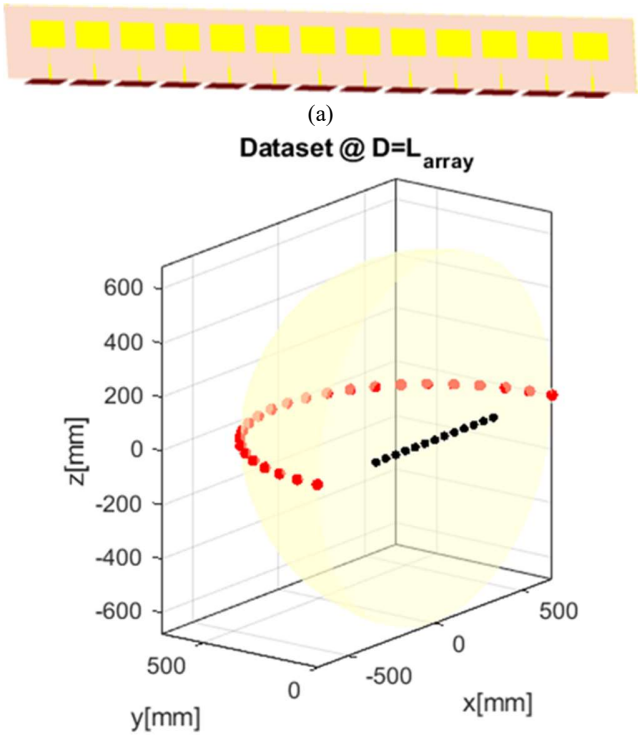

Fig. 2. 1-D AUT: CST design [subplot(a)]; measurement points (red dots) and array elements location (black dots) [subplot(b)].

III.A. RSER evaluation in the case of ON-OFF faults for both linear and planar AUTs

To accurately evaluate the ultimate capabilities of the proposed approach, the RSER has been determined by running the diagnostic procedure for the detection of ON-OFF faults in different noisy scenarios for very many values of S and M. In particular, for each value of S, we considered multiple different M/S instances and, for every single case, we repeated the diagnostics 500 times by randomly changing the location of both the faulty elements and the measurement samples. Then, to generate the RSER plots, only the experiments leading to an NMSE lower than a very small threshold have been considered successful.

Coming to details, both linear and planar arrays have been considered as AUTs. In both cases, to mitigate the effect of truncation errors [31], a hemispheric scanning surface has been exploited for three different distances D from the AUT, namely, $D = d * L_{array}$, with $d = [0.5; 1; 1.5]$ and L_{array} being the overall (maximum) size of the AUT. For this kind of scanning surface, the tangential components of the field are E_θ and E_φ.

The 1-D AUT is shown in Fig. 2(a). It has L_{array} =5.44λ (λ denoting the wavelength) and it is composed of 13 equally-spaced patch antennas working at 2.45 GHz and built as reported in [27]. The M phaseless near-field measurements were randomly chosen among the 24 independent samples [33] of E_θ (which was the dominant component) on a semicircle in front of the antenna [see Fig. 2(b)].

The achieved RSER as a function of the ratio M/S is shown in Fig. 3 for S=1 and S=2. As it can be seen, $M = 4S$ and $M = 5S$ ensure, respectively, RSER>80% for $d = [1; 1.5]$ and $d = 0.5$. Equivalent results (which are not shown for the sake of brevity) have been achieved for S=3.

The improvement in the RSER experienced as D increases, which will emerge again in the next presented test cases, agrees with the fact that the farther the measurement probes the better the fulfillment of the conditions enabling the CS theory.

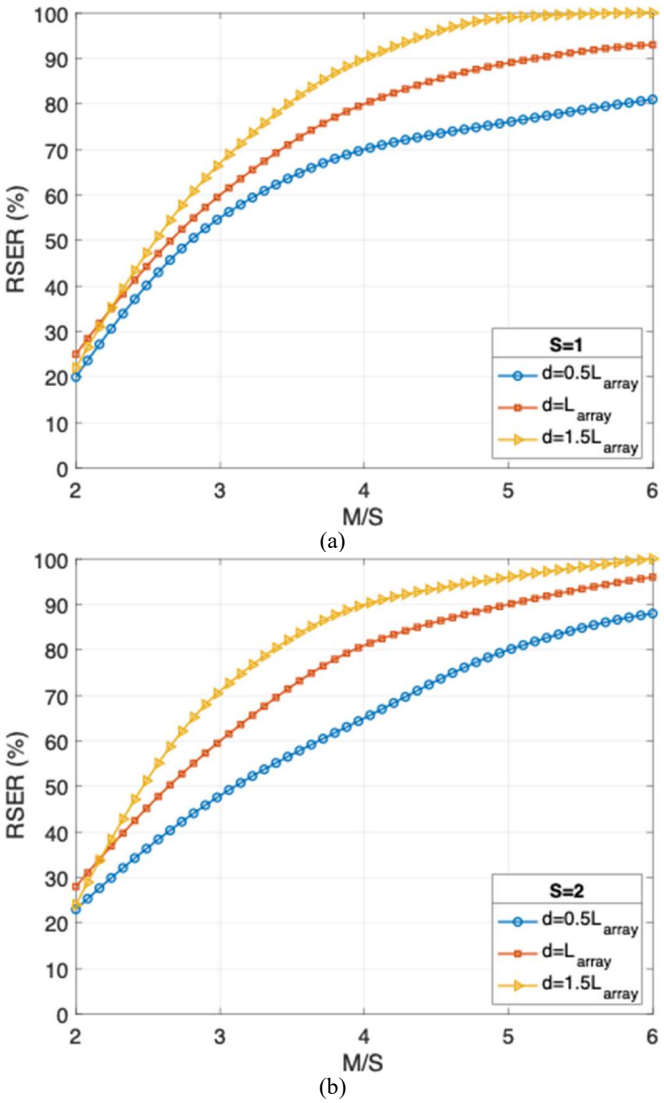

Fig. 3. Diagnosis of the AUT shown in Fig. 2(a): RSER performance achieved for $S = 1$ [subplot(a)] and $S = 2$ [subplot(b)] considering different values of the ratio M/S and different AUT-probe distances.

The RSER analysis has been repeated by corrupting the data with white Gaussian noise leading to signal-to-noise ratios (SNRs) respectively equal to 30 dB and 25 dB. The outcomes, which are reported in Fig. 4 for $D = L_{array}$ and $S = 2$, show a good agreement with the same kind of analysis performed in [10] where, however, only far-field measurements were used.

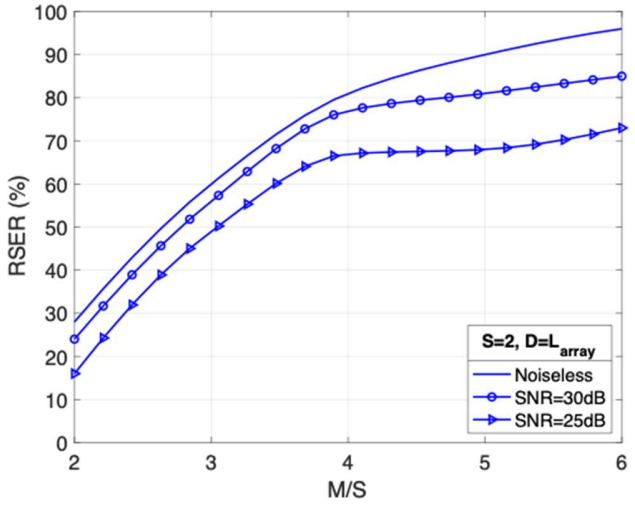

Fig. 4. Fault diagnosis of the 1-D AUT shown in Fig. 2(a): RSER performance for $S = 2$ and $D = L_{array}$ in the presence of noise with SNR=30 dB and SNR=25 dB as compared to the noiseless results shown in Fig. 3(b).

A further set of experiments has been performed by considering the 2-D AUT shown in Fig. 5(a). It is a $5\lambda \times 2.5\lambda$ planar array composed of 25 WR-90 waveguides working at 10 GHz and built as reported in [11].

The phaseless near-field measurements have been randomly chosen amongst the 200 independent samples [33] on a hemisphere designed as dictated by [34] and depicted in Fig. 5(b). In this case, since both the tangential field components E_θ and E_φ have a significant intensity, the array diagnostics has been performed by simultaneously exploiting both components (leading to the results depicted in Fig. 6) as well as by resorting to one component at a time (generating the outcomes shown in Fig. 7)[6]. As it can be seen, in the first case, using $4S$ measurement points allows achieving:

- RSER≈90% regardless of the probe-AUT distance and the number of faults;
- RSER≈100% for S>1 and $D \geq L_{array}$.

These outcomes confirm the effectiveness of the proposed procedure[7]. Furthermore, high diagnostics performances have been achieved even in the case where only one component of the field is exploited. In fact, as shown in Fig. 7, $M = 6S$ ensures RSER>95% if only E_φ is exploited as well as RSER>80% if just E_θ is used.

[6] Both field components can be measured at the same points of the scanning surface, which has the double advantage of reducing the probe's movement and doubling the amount of data. In fact, in this case the actual number of data (denoted by M from now on) results twice the number of measurement points (denoted by $\overline{M}$ from now on).

Finally, some of the experiments relative to Fig. 6 have been repeated in the presence of noise. The outcomes are summarized in Fig. 8 and demonstrate that faults can also be detected by experiencing an acceptable reduction in the RSER, i.e., 10% (for SNR=30 dB) and 20% (for SNR=25 dB).

As a final set of numerical experiments, the diagnostic technique has been assessed on a much larger array. Hence, a planar AUT composed of 121 elements has been considered (keeping the same radiating elements, interelement spacing, and operating frequency as the ones considered in the previous test case). The distance D of the hemispherical scanning surface was modified according to the actual size of the larger AUT, and the measurement points were randomly selected among the independent sampling points (which turn out to be equal to 968 due to the rules in [33]).

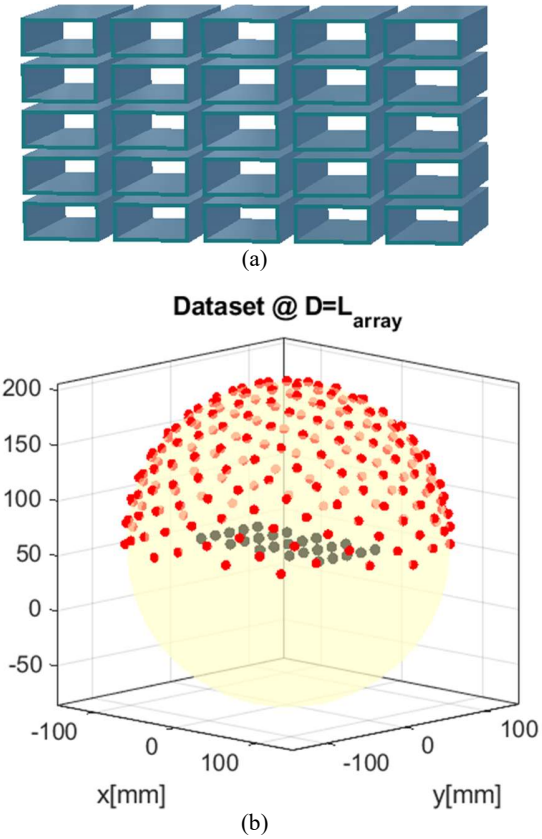

Fig. 5. 2-D AUT: CST design [subplot(a)]; measurement points location (red dots) and array elements location (green dots) [subplot(b)].

The achieved results are reported in Fig. 9. Notably, when jointly processing E_θ and E_φ, using $4S$ measurement points ensures RSER≈100%. An equivalent performance (not shown here for the sake of brevity) has been achieved by exploiting only one component of the field and $6S$ measurement points.

[7] All results shown throughout Section III must be evaluated by taking into account the fact that, according to the CS theory (see also [11]), $4S$ is the minimum number of real-valued measurements required for the correct retrieval of a S-sparse signal.

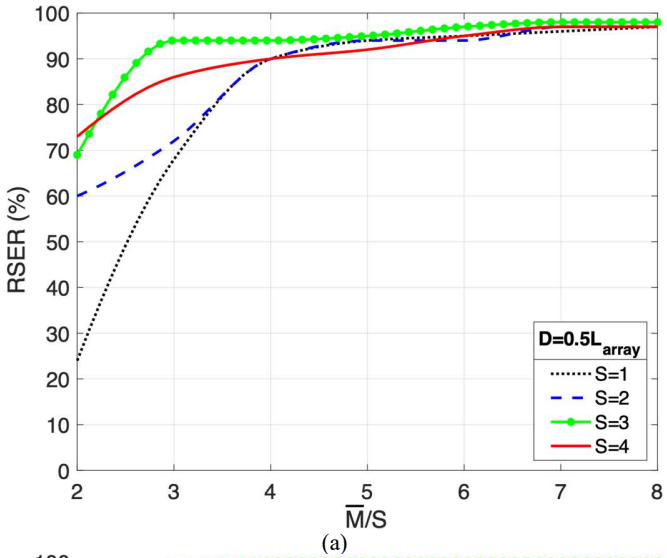

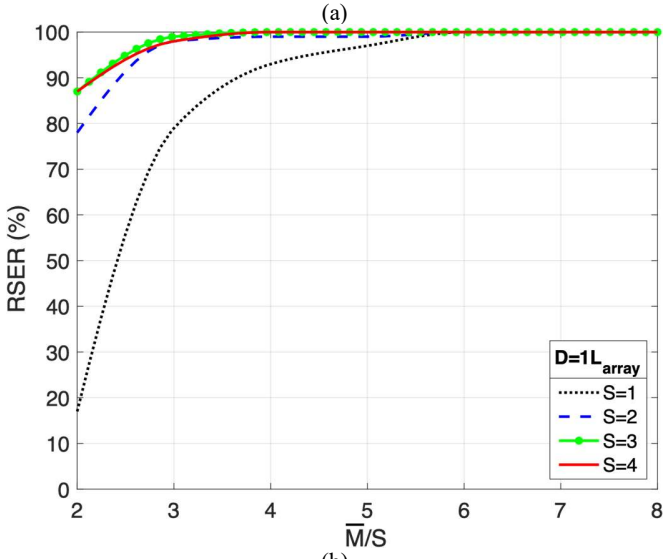

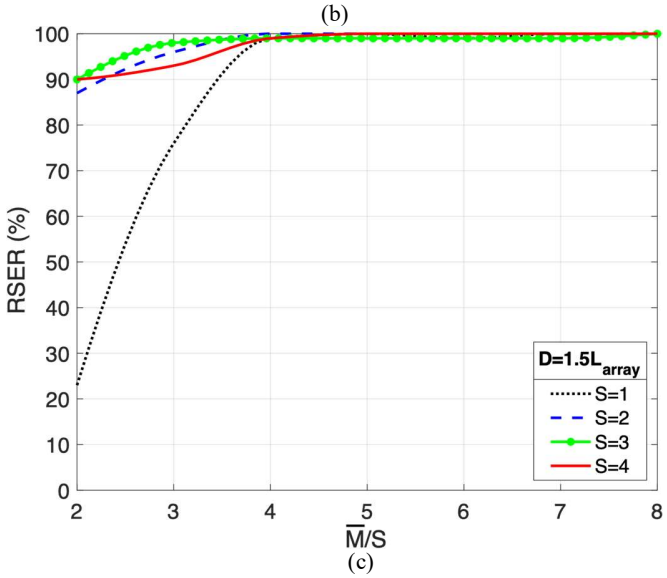

Fig. 6. Outcomes of the diagnosis of the AUT of Fig. 5(a) by using both E_θ and E_φ for $S = [1; 2; 3; 4]$ and different AUT-probe distances, i.e., $D = 0.5L_{array}$ [subplot(a)], $D = L_{array}$ [subplot(b)], and $D = 1.5L_{array}$ [subplot(c)]. $\overline{M}$ denotes the number of measurement points.

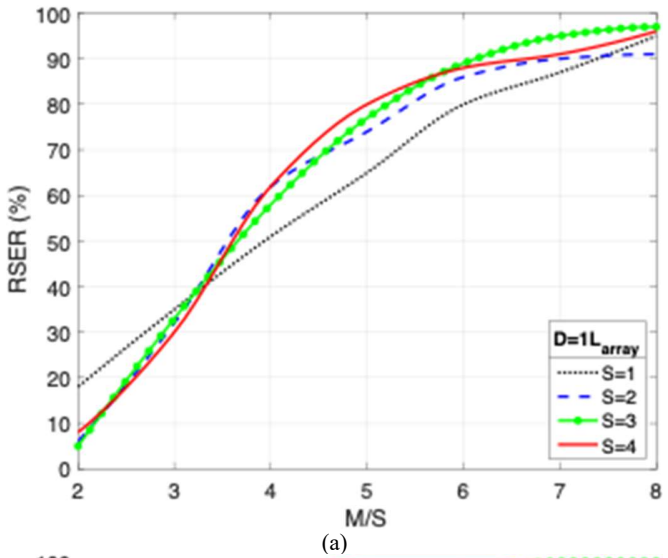

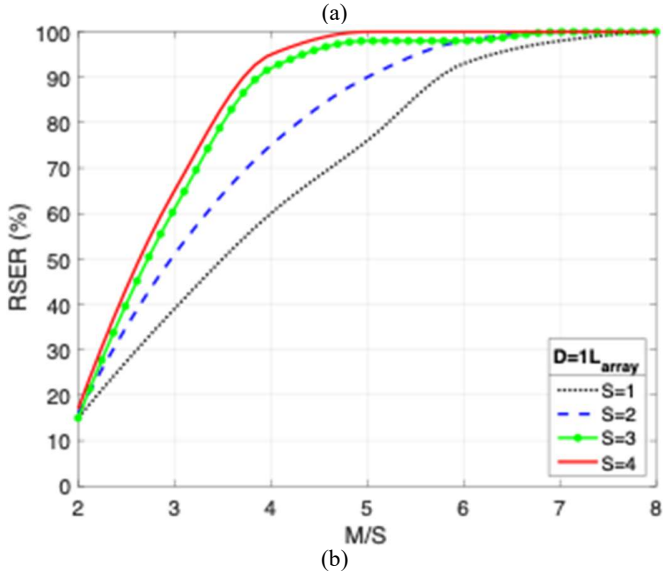

Fig. 7. Fault diagnosis of the AUT of Fig. 5(a): RSER as a function of the ratio M/S for $S = [1; 2; 3; 4]$ and $D = L_{array}$ achieved by using only E_θ [subplot(a)] and by using only E_φ [subplot(b)].

These outcomes corroborate the effectiveness of the proposed procedure in detecting ON-OFF faults for large AUTs. In particular, despite the new array is approximately 5 times larger (in terms of number of elements) than the previous one, the proposed technique resulted still able to detect the faults by exploiting a reduced amount of data.

To evaluate the impact on the diagnosis of the distance between the measurement surface and the AUT, the RSERs achieved for different probe–AUT distances are superimposed in figures 10 and 11 for the smallest and largest AUTs, respectively. Notably, using $4S$ measurement points allows achieving RSER≈100% in all experiments involving the 121-elements array whatever the D value, as well as in all experiments dealing with the 25-elements array provided that $D \geq L_{array}$. Besides confirming the capability to detect the failures even at a measurement distance as close as half as the AUT size, these results reveal that, on the 121-elements array,

the proposed approach worked even better than what it did for the 25-elements array.

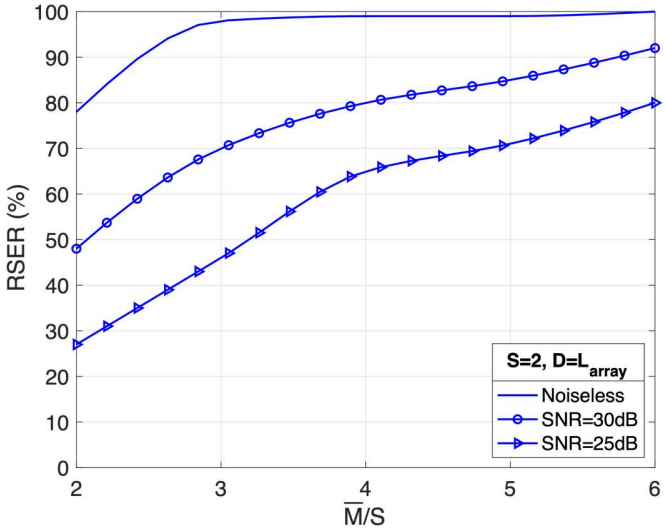

Fig. 8. Fault diagnosis of the 25-elements planar AUT shown in Fig. 5(a) by processing M square amplitude samples of both E_θ and E_φ. RSER performance for $S = 2$ and $D = L_{array}$ in presence of noisy with SNR=30 dB [circular maker] and SNR=25 dB [triangular marker]. The continuous line represents the RSER of the corresponding noiseless case shown in Fig. 6(b).

III.B. ON-OFF failure detection for a 2-D AUT using a different kind of measurement surface

It is common practice to address the fault diagnosis problem by considering planar scanning surfaces in front of the AUT [12]–[14],[16]–[18]. In this respect, we tested the proposed approach in the case of ON-OFF faults (i.e., by setting the excitations of S elements to zero) on both the planar waveguide arrays described in the previous subsection.

Coming to details, as far as the 25-elements AUT is concerned, we first performed the diagnostics of $S = 3$ faults by considering $\overline{M} = 6$ amplitude-only near-field measurement points randomly chosen among 325 samples uniformly distributed on a planar surface as large as $6\lambda \times 3.5\lambda$ and placed 5λ from the AUT. Then, we repeated the experiment two more times by using noisy data with SNR=30 dB and SNR=25 dB, exploiting $\overline{M} = 9$ near-field phaseless measurement points. The achieved results are shown in Fig. 12 and, again, prove the effectiveness and accuracy of the diagnostic approach even if noise is present in the data and truncation errors occur due to the type of scanning surface. The above statement is corroborated by the NMSE associated with each numerical test, i.e.: $1.5\text{x}10^{-9}$ for the noiseless case (revealing a perfect fault detection), 0.027 when SNR=30 dB, and 0.050 when SNR=25 dB.

The same kind of analysis was carried out for the 121-elements AUT. In this case, the planar scanning surface, $6\lambda \times 3.5\lambda$ large and placed 5λ from the AUT, was uniformly sampled into 325 points. Among these, to perform the accurate detection of $S = 3$ faults, $\overline{M} = 15$ points were randomly selected for both the noiseless case and the noisy case with SNR=35 dB, and $\overline{M} = 18$ points were randomly selected for the noisy case with SNR=30 dB. Conversely, when $S = 5$ faults were present, the accurate faults detection required $\overline{M} = 20$ for both the noiseless case and the noisy case with SNR=35 dB, and $\overline{M} = 25$ for the noisy case with SNR=30 dB. Fig. 13 shows the faults retrieval in the cases of S=3 [subplot (a)] and S=5 [subplot (b)]. The amplitude of the retrieved excitations is quite high in correspondence with the actual faults, thus allowing their detection with good accuracy. In fact, for S=3, we obtained a perfect detection of the faults (i.e., NMSE=$2.5\text{x}10^{-10}$) in the noiseless case, and a very good performance also in the presence of noise (i.e., NMSE=0.078 for SNR=35 dB, NMSE=0.16 for SNR=30 dB). Similarly, for S=5, we obtained a perfect reconstruction of the faults (i.e., NMSE=$2.4\text{x}10^{-11}$) in the noiseless case, and a very good performance also in the noisy case (i.e., NMSE=0.075 for SNR=35 dB, NMSE=0.16 for SNR=30 dB).

III.C. Phase fault detection and comparison with [18]

The detection of phase faults is addressed in this subsection. As stated above, only one recent approach was able to solve this problem by exploiting only near-field phaseless measurements, i.e., the technique in [18].

To compare the proposed approach with such a technique, we considered the same AUT as the one in [18] and the same faults, i.e., a $2.9\lambda \times 2.4\lambda$ planar array composed of $N = 25$ dipoles with $S = 3$ π-phase faults. Furthermore, we kept the measurement surface and the AUT-probes distance unchanged with respect to [18], i.e., a $3\lambda \times 3\lambda$ planar surface placed 0.9λ from the AUT. Finally, as in [18], we corrupted the data with white Gaussian noise leading to an SNR=20 dB.

The phase of the reconstructed excitations following the procedure in Section II.B and adopting $M = 90$ phaseless near-field data is shown in Fig. 14(a). As it can be seen, the faults have been correctly identified (NMSE=0.0043). Therefore, the proposed approach resulted able to correctly detect the same antenna failures as in [18] while reducing the number of required measurements by approximately 90%. In particular, our technique required only 90 measurements to achieve the same diagnostic performance that in [18] required 961 measurements.

Finally, to test the proposed approach in a more challenging scenario, we repeated the experiment by considering random (and smaller) phase faults (which are not dealt with in [18]). The achieved results are shown Fig. 14(b), where again, one can notice that the faults have been detected in an accurate fashion (NMSE=0.0036).

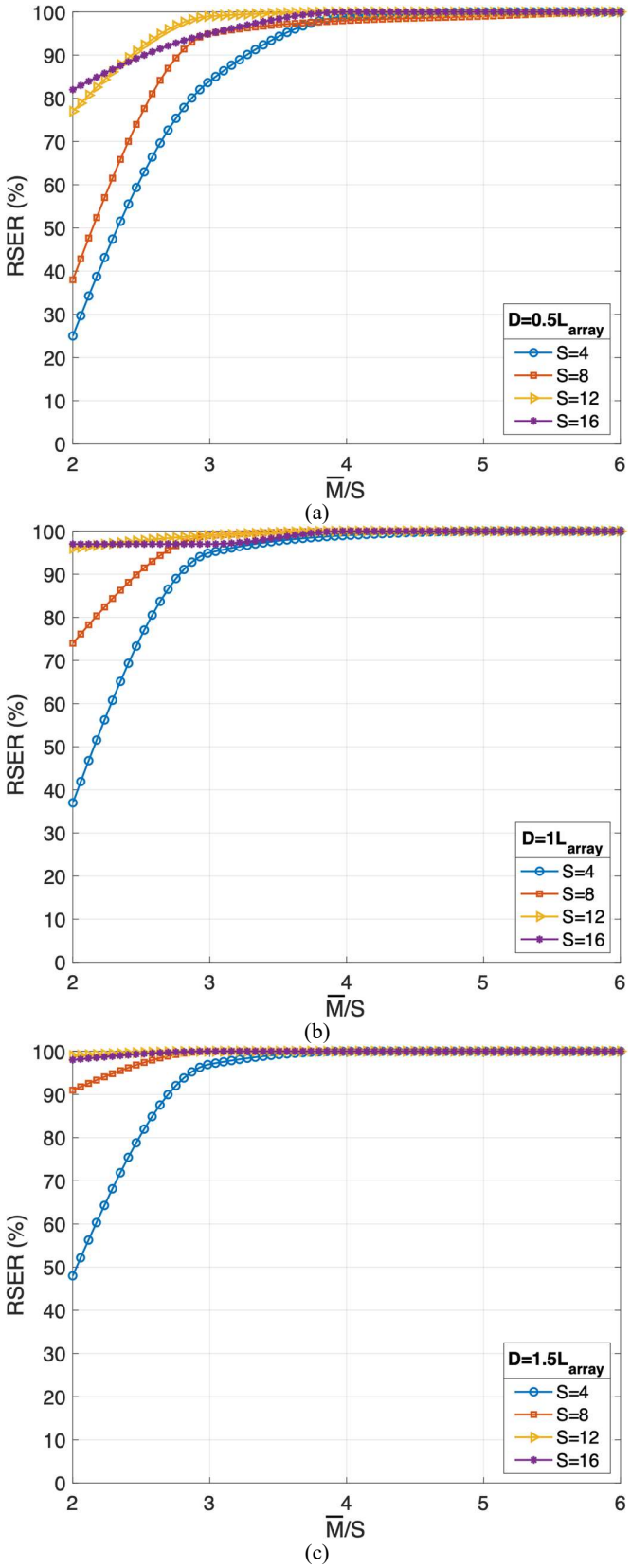

Fig. 9. Outcomes of the diagnosis of the 121-elements planar AUT by using both E_θ and E_φ for $S = [4; 8; 12; 16]$ and different AUT-probe distances: $D = 0.5L_{array}$ [subplot(a)]; $D = L_{array}$ [subplot(b)]; $D = 1.5L_{array}$ [subplot(c)]. $\overline{M}$ denotes the number of measurement points.

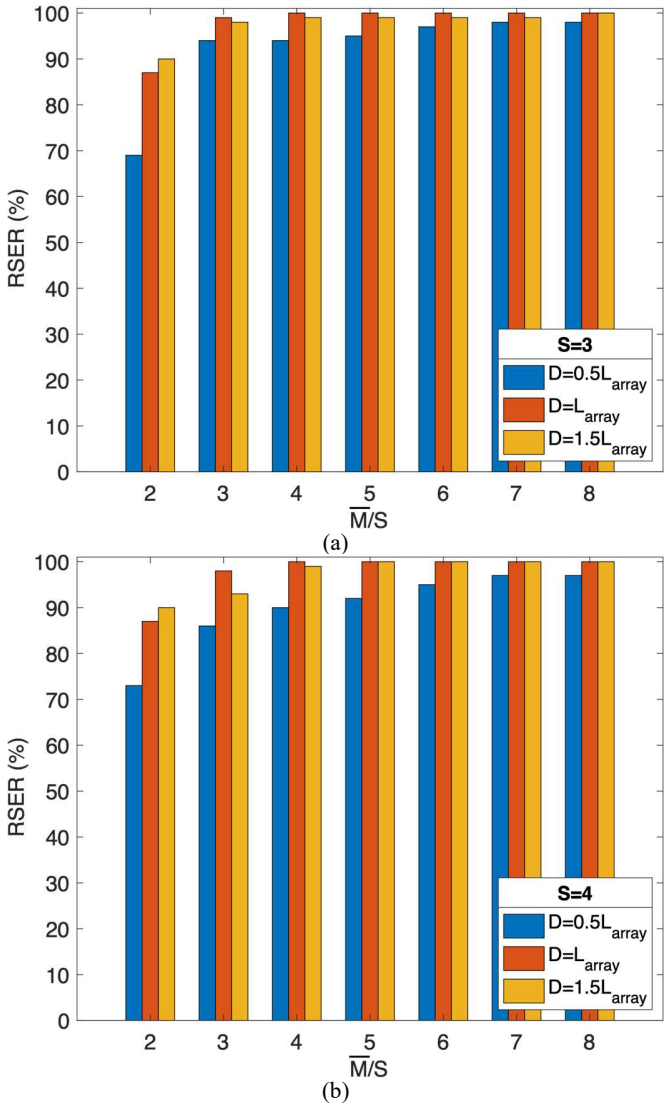

Fig. 10. Fault diagnosis of the 25-elements AUT shown in Fig. 5(a) using both E_θ and E_φ: RSER as a function of $\overline{M}/S$ ($\overline{M}$ denoting the number of measurement points) for $d = [0.5; 1; 1.5]$ and different number of faults, i.e., $S = 3$ [subplot (a)] and $S = 4$ [subplot (b)].

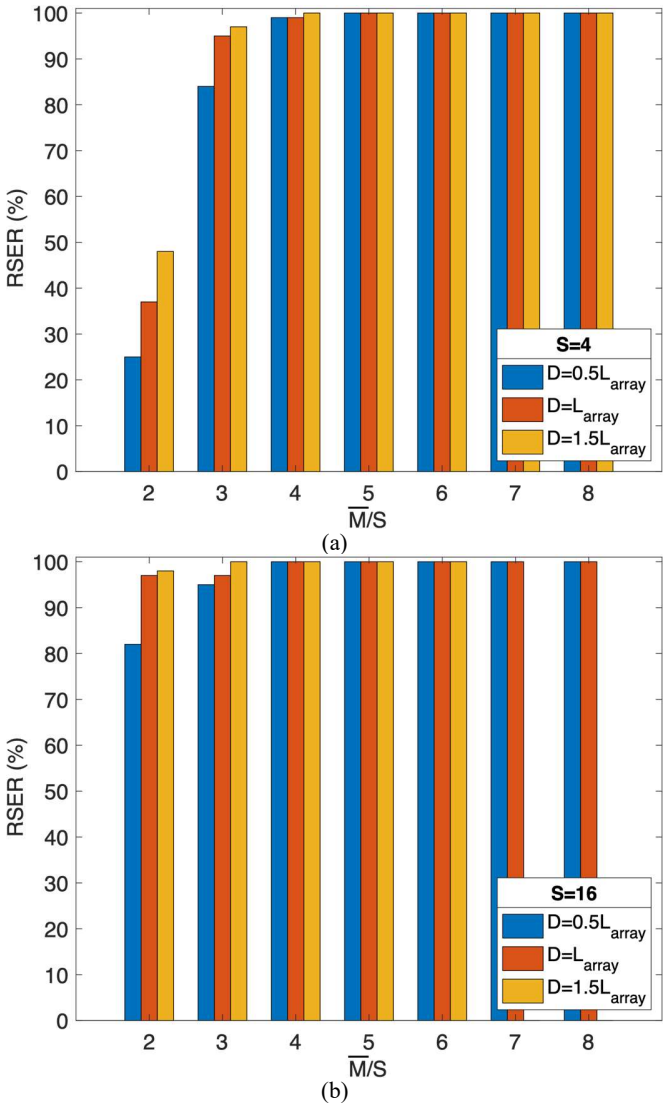

Fig. 11. Fault diagnosis of the 121-elements planar AUT by using both E_θ and E_φ: RSER as a function of $\overline{M}/S$ ($\overline{M}$ denoting the number of measurement points) for $D = [0.5; 1; 1.5] * L_{array}$ and different number of faults, i.e., $S = 4$ [subplot (a)] and $S = 16$ [subplot (b)].

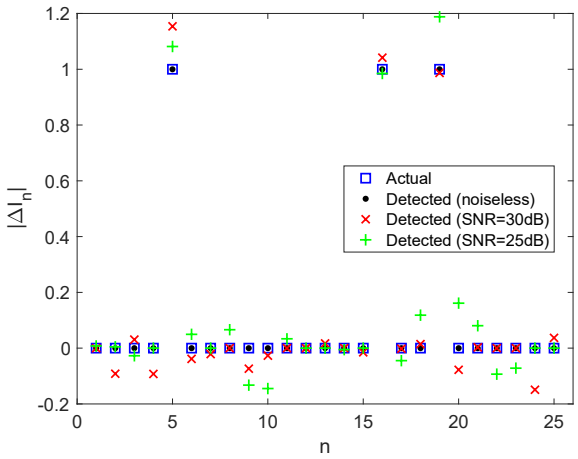

Fig. 12. Diagnostics of S=3 ON-OFF faults on the AUT shown in Fig. 5(a) by using both E_x and E_y and a planar scanning surface: amplitude of the "differential" AUT excitations retrieved for $\overline{M} = 6$ and $\overline{M} = 9$, respectively, in case of noiseless data and noisy data ($\overline{M}$ denoting the number of measurement points).

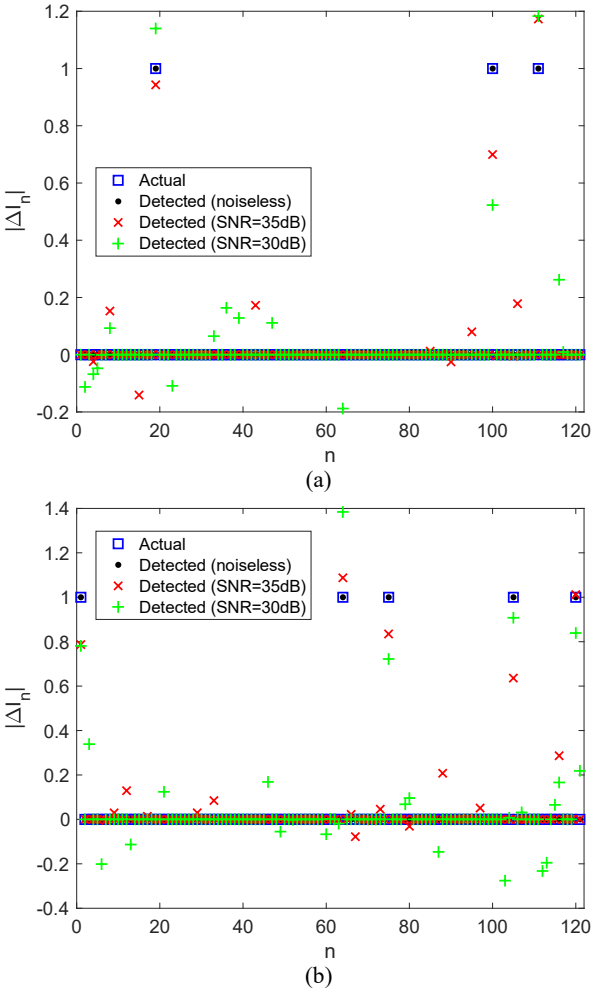

Fig. 13. Diagnostics of ON-OFF faults on a 121-elements planar AUT by using both E_x and E_y taken on a planar scanning surface. Subplot (a): amplitude of the "differential" AUT excitations retrieved for $S = 3$ by exploiting $\overline{M} = 15$ near-field phaseless measurement points in case of noiseless data and noisy data with SNR=35 dB, and $\overline{M} = 18$

near-field phaseless measurement points in case of noisy data with SNR=30 dB. Subplot (b): amplitude of the "differential" AUT excitations retrieved for $S = 5$ by exploiting $\overline{M} = 20$ near-field phaseless measurement points in case of noiseless data and noisy data with SNR=35 dB, $\overline{M} = 25$ near-field phaseless measurement points in case of noisy data with SNR=30 dB.

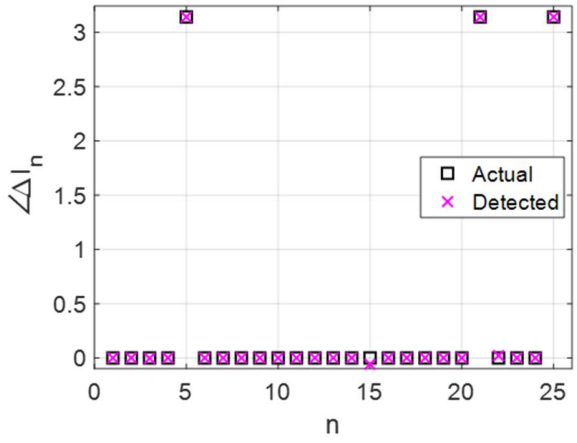

(a)

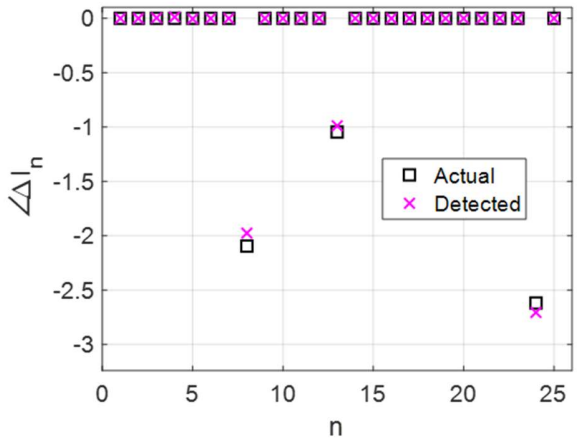

(b)

Fig. 14. Diagnostics of *S*=3 phase-faults on a planar array of dipoles: comparison with [18]. Phase of the "differential" AUT excitations retrieved by using $M = 90$ noisy (SNR=20 dB) phaseless data in two different cases: uniform π phase faults [subplot(a)]; random phase faults [subplot(b)].

IV. Experimental Validation

In the following, we present an experimental validation of the proposed approach. This was done by using the antenna developed in [14] as AUT, which is also shown in Fig. 15. In particular, the AUT is a slotted waveguide array with a length of 12λ and is composed of $N = 14$ radiating elements. The operating frequency is 10 GHz.

In [14], the near-field of this AUT was measured in an anechoic chamber to perform the diagnostics of $S = 2$ failures realized by covering the 3rd and 11th slots with a conductive material. In particular, 41×41 $\lambda/2$-spaced measurements were taken on a planar surface placed 40 cm away from the AUT by using a rectangular waveguide as the measuring probe.

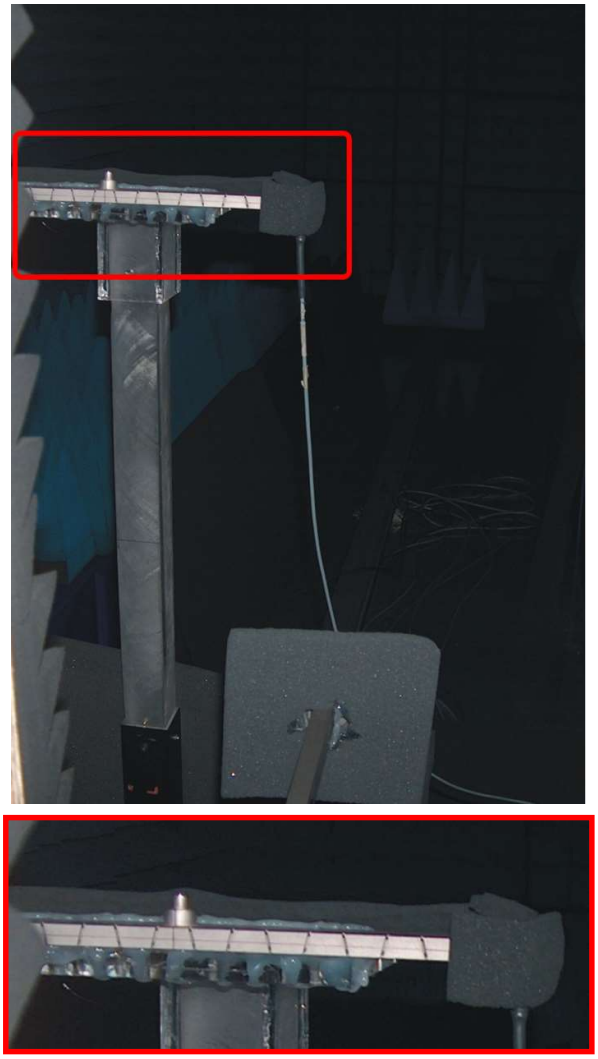

Fig. 15. Photo of the slotted-waveguide array into the anechoic chamber at University of Calabria. The rectangular waveguide used as measuring probe is also visible at the bottom.

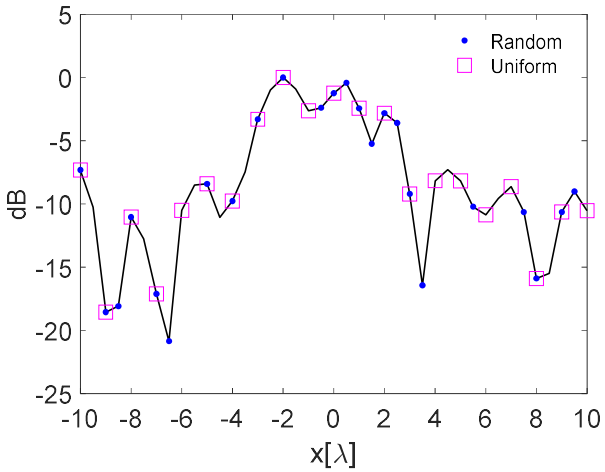

Fig. 16. Near-field amplitude of the AUT shown in Fig. 15 in the presence of $S = 2$ failures, i.e., 3rd and 11th non-radiating elements, as measured inside anechoic chamber through two different sampling strategies: uniform sampling ($M = 21$, magenta squares); random sampling ($M = 24$, blue dots).

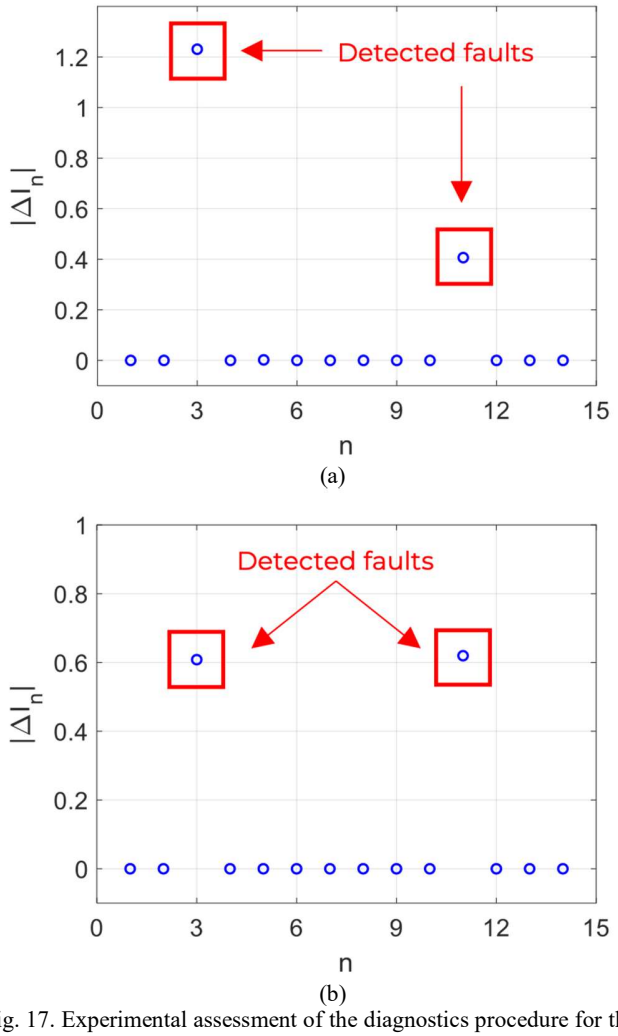

Fig. 17. Experimental assessment of the diagnostics procedure for the AUT shown in Fig. 15: amplitudes of the "differential" AUT excitations retrieved by using, respectively, $M = 21$ uniformly-distributed phaseless samples [subplot (a)] and $M = 24$ randomly-distributed phaseless samples [subplot (b)].

Notably, while amplitude and phase measurements were used in [14], the diagnostics experiment was repeated here by measuring, inside the anechoic chamber, only the amplitude of the near field.

In detail, we applied the procedure described in subsection II.C to perform the diagnostics in two different cases, i.e., by exploiting $M = 21$ uniformly distributed near-field phaseless samples and $M = 24$ randomly distributed near-field phaseless samples.

The near-field amplitude measured in the two cases along the central line of the acquisition domain is shown in Fig. 16, while the corresponding diagnostic outcomes are reported in Fig. 17. As it can be seen, even if the number of exploited measurements is much lower than the number of degrees of freedom of the square-amplitude field generated by the AUT (which results approximately to 49), the two faults have been correctly detected in both cases. This circumstance confirms the actual effectiveness of the proposed technique in real-world applications.

V. Conclusions

A new and effective approach to the fault diagnosis of array antennas has been presented, assessed, and experimentally validated. The technique exploits amplitude-only near-field data and makes no restrictions on the array structure.

Some systematic comparisons of the proposed approach with other near-field techniques that use either phaseless or amplitude and phase measurements are summarized in Tab. I. In summary, the proposed approach has several advantages over other techniques, as follows:

- it is one of the only three techniques (the other ones being [8] and [18]) able to perform the diagnostics by resorting only to phaseless near-field data, and it is the only one that has undergone experimental validation;
- it accomplishes fault diagnostics by exploiting a reduced number of measurements. In particular, it achieves high RSER performances even by using $4S$ measurements which, in turn, by virtue of the CS theory, is the lowest admissible number of measurements if phaseless data are exploited. In fact, since that at least 2S complex-valued measurements are required to identify S faulty elements, and one complex-valued measurement is equivalent to two real-valued measurements, at least $4S$ phaseless measurements are required to perform the exact recovery of an S-sparse signal (see [11] and the references cited therein);
- it handles whatever kind of radiating elements, from dipoles (which are the most used, see [12],[13],[16]–[18]) to patches (as in [8] and [12]), waveguides, and slots, arranged in both linear and planar geometries;
- as far as the size of the AUT is concerned, it compares well with other works, and it was applied to larger AUTs with respect to [8] and [18];
- it shows good performance in the presence of noise.

As shown through an experimental validation and an extensive set of full-wave electromagnetic simulations, the presented diagnostics procedure results fast and effective in real-world applications and hence can be relevant to current high-performance arrays such as those designed, for instance, in [35]–[37].

Due to the adoption of phaseless data, the presented technique is also strictly related to phase retrieval (PR). In fact, the circumstance that the diagnostic results achieved in the case of planar arrays are even better than those obtained for one-dimensional arrays agrees with the fact that 2-D PR problems are usually easier to solve with respect to 1-D problems (due to the presence, in the latter case, of different complex fields all having the same square-amplitude distribution) [38].

References

[1] M. D. Migliore, "Array diagnosis from far-field data using the theory of random partial Fourier matrices," *IEEE Antennas Wireless Propag. Lett.*, vol. 12, pp. 745-748, 2013.

[2] Y. Zhang and H. Zhao, "Failure diagnosis of a uniform linear array in the presence of mutual coupling," *IEEE Antennas Wireless Propag. Lett.*, vol. 14, pp. 1010-1013, 2015.

[3] B. Fuchs, L. Le Coq, and M. D. Migliore, "Fast antenna array diagnosis from a small number of far-field measurements," *IEEE Trans. Antennas Propag.*, vol. 64, n. 6, pp. 2227-2235, 2016.

[4] T. Ince and G. Ögücü, "Array failure diagnosis using nonconvex compressed sensing," *IEEE Antennas Wireless Propag. Lett.*, vol. 15, pp. 992-995, 2016.
[5] W. Li, W. Deng, and M. D. Migliore, "A deterministic far-field sampling strategy for array diagnosis using sparse recovery," *IEEE Antennas Wireless Propag. Lett.*, vol. 17, n. 7, pp. 1261-1265, 2018.
[6] M. Salucci, A. Gelmini, G. Oliveri, and A. Massa, "Planar array diagnosis by means of an advanced Bayesian compressive processing," *IEEE Trans. Antennas Propag.*, vol. 66, no. 11, pp. 5892-5906, 2018.
[7] O. M. Bucci, A. Capozzoli, and G. D'Elia, "Diagnosis of array faults from far-field amplitude-only data," *IEEE Trans. Antennas Propag.*, vol. 48, no. 5, pp. 647-652, 2000.
[8] O. M. Bucci, A. Capozzoli, and G. D'Elia, "A method for the diagnosis of phase faults in array antennas from amplitude only field data," *IEEE Antennas Propag. Soc. Symp. & USNC/URSI Radio Sci. Meet.* vol. 4, pp. 2238-2241, 2000.
[9] B. Fuchs and L. Le Coq, "Excitation retrieval of microwave linear arrays from phaseless far-field data," *IEEE Trans. Antennas Propag.*, vol. 63, n. 2, pp. 748-754, 2015.
[10] A. F. Morabito, R. Palmeri, and. T. Isernia, "A compressive-sensing-inspired procedure for array antenna diagnostics by a small number of phaseless measurements," *IEEE Trans. Antennas Propag.*, vol. 64, n. 7, pp. 3260-3265, 2016.
[11] R. Palmeri, T. Isernia, and A. F. Morabito, "Diagnosis of planar arrays through phaseless measurements and sparsity promotion," *IEEE Antennas Wireless Propag. Lett.*, vol. 18, n. 6, pp. 1273-1277, 2019.
[12] O. M. Bucci, M. D. Migliore, G. Panariello, and P. Sgambato, "Accurate diagnosis of conformal arrays from near-field data using the matrix method," *IEEE Trans. Antennas Propag.*, vol. 53, n. 3, pp. 1114-1120, 2005.
[13] M. D. Migliore, "A compressed sensing approach for array diagnosis from a small set of near-field measurements," *IEEE Trans. Antennas Propag.*, vol. 59, n. 6, pp. 2127-2133, 2011.
[14] S. Costanzo, A. Borgia, G. Di Massa, D. Pinchera, and M. D. Migliore, "Radar array diagnosis from undersampled data using a compressed sensing/sparse recovery technique," *J. Electr. Comput. Eng.*, vol. 2013, Article ID 627410, 2013.
[15] K. Konno, S. Asano, T. Umenai, and Q. Chen, "Diagnosis of array antennas using eigenmode currents and near-field data", *IEEE Trans. Antennas Propag.*, vol. 66, n. 11, pp. 5982-5989, 2018.
[16] C. Xiong, G. Xiao, Y. Hou, and M. Hameed, "A compressed sensing-based element failure diagnosis method for phased array antenna during beam steering," *IEEE Antennas Wireless Propag. Lett.*, vol. 18, n. 9, pp. 1756-1760, 2019.
[17] Z. Lin, Y. Chen, X. Liu, R. Jiang, and B. Shen, "A bayesian compressive sensing-based planar array diagnosis approach from near-field measurements," *IEEE Antennas Wireless Propag. Lett.*, vol. 20, n. 2, pp. 249-253, 2021.
[18] X. Wang, K. Konno, and Q. Chen, "Diagnosis of array antennas based on phaseless near-field data using artificial neural network," *IEEE Trans. Antennas Propag.*, vol. 69, no. 7, pp. 3840-3848, 2021.
[19] J. Laviada Martínez, A. Arboleya-Arboleya, Y. Álvarez-López, C. García-González, and F. Las-Heras, "Phaseless antenna diagnostics based on off-axis holography with synthetic reference wave," *IEEE Antennas Wireless Propag. Lett.*, vol. 13, pp. 43-46, 2014.
[20] M. G. Fernández, Y. Á. López, and F. L. Andrés, "Antenna measurement and diagnostics processing techniques using unmanned aerial vehicles," *2019 13th Eur. Conf. Antennas Propag. (EuCAP)*, pp. 1-5, 2019.
[21] G. Hislop, L. Li, and A. Hellicar, "Phase retrieval for millimeter and submillimeter-wave imaging," *IEEE Trans. Antennas Propag.*, vol. 57, n. 1, pp. 286–289, 2009.
[22] G. Junkin, T. Huang, and J. Bennett, "Holographic testing of terahertz antennas," *IEEE Trans. Antennas Propag.*, vol. 48, n. 3, pp. 409–417, 2000.
[23] E. J. Candès, J. K. Romberg, and T. Tao, "Robust uncertainty principles: exact signal reconstruction from highly incomplete frequency information," *IEEE Trans. Inf. Theory*, vol. 52, n. 2, pp. 489-509, 2006.
[24] R. G. Yaccarino, and Y. Rahmat-Samii, "Phaseless bi-polar planar near-field measurements and diagnostics of array antennas," *IEEE Trans. Antennas Propag.,* vol. 47, no. 3, pp. 574-583, 1999.
[25] Y. Álvarez, F. Las-Heras, and M. R. Pino, "Antenna diagnostics using phaseless NF information", *Automatika*, vol. 53, n. 1, pp. 49-55, 2012.
[26] A. F. Morabito, R. Palmeri, V. A. Morabito, A. R. Laganà, and T. Isernia, "Single-surface phaseless characterization of antennas via hierarchically ordered optimizations," *IEEE Trans. Antennas Propag.*, vol. 67, n. 1, pp. 461-474, 2018.
[27] A. F. Morabito, A. Di Carlo, L. Di Donato, T. Isernia, and G. Sorbello, "Extending spectral factorization to array pattern synthesis including sparseness, mutual coupling, and mounting-platform effects," *IEEE Trans. Antennas Propag.*, vol. 67, n. 7, pp. 4548-4559, 2019.
[28] F. R. Varela, J. F. Álvarez, B. G. Iragüen, M. S. Castañer, and O. Breinbjerg, "Numerical and experimental investigation of phaseless spherical near-field antenna measurements," *IEEE Trans. Antennas Propag.*, vol. 69, no. 12, pp. 8830-8841, 2021.
[29] J. Knapp, A. Paulus, and T. F. Eibert, "Reconstruction of squared field magnitudes and relative phases from magnitude-only near-field measurements," *IEEE Trans. Antennas Propag.*, vol. 67, n. 5, pp. 3397-3409, 2019.
[30] M. Salucci, M. D. Migliore, P. Rocca, A. Polo, and A. Massa, "Reliable antenna measurements in a near-field cylindrical setup with a sparsity promoting approach," *IEEE Trans. Antennas Propag.n*, vol. 68, n. 5, pp. 4143-4148, 2020.
[31] A. C. Newell, "Error analysis techniques for planar near-field measurements," *IEEE Trans. Antennas Propag.,* vol. 36, no. 6, pp. 754-768, 1988.
[32] CST Studio Suite 3D EM simulation and analysis software (2022) [Software] https://www.3ds.com/products-services/simulia/products/cst-studio-suite.
[33] O. M. Bucci, C. Gennarelli, and C. Savarese, "Representation of electromagnetic fields over arbitrary surfaces by a finite and nonredundant number of samples," *IEEE Trans. Antennas Propag.,* vol. 46, no. 3, 351-359, 1998.
[34] R. Marques, C. Bouville, M. Ribardière, L. P. Santos, and K. Bouatouch, "Spherical Fibonacci point sets for illumination integrals," *Comput. Graph. Forum*, vol. 32, no. 8, pp. 134-143, 2013.
[35] O. M. Bucci, T. Isernia, A. F. Morabito, S. Perna, and D. Pinchera, "Aperiodic arrays for space applications: An effective strategy for the overall design," 2009 3rd European Conference on Antennas and Propagation, Berlin, Germany, 2009, pp. 2031-2035.
[36] O. Leonardi, M. G. Pavone, G. Sorbello, A. F. Morabito, and T. Isernia, "Compact single-layer circularly polarized antenna for short-range communication systems," *Microw. Opt. Technol. Lett.*, vol. 56, n. 8, pp. 1843–1846, 2014.
[37] R. Palmeri, M. T. Bevacqua, A. F. Morabito, and T. Isernia, "Design of artificial-material-based antennas using inverse scattering techniques," *IEEE Trans. Antennas Propag.*, vol. 66, n. 12, pp. 7076–7090, 2018.
[38] R. Palmeri, G. M. Battaglia, A. F. Morabito and T. Isernia, "Reflector antennas characterization and diagnostics using a single set of far-field phaseless data and crosswords-like processing," *IEEE Trans. Antennas Propag.*, vol. 70, n. 9, pp. 8424-8439, 2022.

Reference	Element type	Array kind and size	Noise on data (lower SNR)	Maximum number of faults	Number of data	Scanning surface	Kind of data
[12] Bucci et al., IEEE TAP 2005	Dipole	Planar: 16 x 64	35dB	Not specified	59 x 129	Planar grid	Amplitude and phase
	Patch	Planar (conformal): 16 x 48	Experimental	Not specified	115 x 95		
[13] Migliore, IEEE TAP 2011	Short dipole	Planar: 17 x 17	35dB	3 (2%)	25	Planar grid	Amplitude and phase
		Planar: 33 x 33		5 (0.5%)	36		
[15] Konno et al., IEEE TAP 2018	Uda Yagi	Linear: 10	Not specified	2 (20%)	Not specified	Cylindrical	Amplitude and phase
	Loop	Linear: 5		1 (20%)	Not specified		
	Uda Yagi	Linear: 2	Experimental	1 (50%)	420		
[16] Xiong et al., IEEE AWPL 2019	Isotropic	Planar: 10 x 10	25dB	15 (10%)	Up to 120	Not specified	Amplitude and phase
[17] Lin et al., IEEE AWPL 2021	Short dipole	Planar: 33 x 33	20dB	108 (10%)	Up to 3000	Planar disk	Amplitude and phase
[18] Wang et al, IEEE TAP 2021	Dipole	Planar: 5 x 5	20dB	3	961	Planar grid	Amplitude-only
	Loop	Planar: 5 x 5					
[8] Bucci et al., APS/URSU Symposium 2000	Patch	Planar: 4 x 4	50dB	3 (20%)	Not specified	Not specified	Amplitude-only
This paper	Patch	Linear: 13		3 (22%)	Up to 18	Hemispherical and planar grid	Amplitude-only
	WR-90 waveguide	Planar: 5 x 5	25dB	4 (16%)	Up to 32		
		Planar: 11 x 11	35dB	12 (10%)	Up to 96		
	Dipole [18]	Planar: 5 x 5 [18]	20dB [18]	3 [18]	90	Planar grid [18]	
	Slot array	Linear: 14	Experimental	2 (15%)	21 or 24	Planar grid	

Tab. 1. Comparison between the proposed diagnostics procedure and the state-of-the-art works dealing with the array faults detection through near-field data.